# Study, design and concept of low frequency SAS

Yan Pailhas,Yvan Petillot and Chris Capus
School of Electrical and Physical Science,
O.S.L., Heriot Watt University,
Edinburgh, EH14 4AS, U.K.
Email: Y.Pailhas@hw.ac.uk

Reg Hollett
Nato Undersea Research Centre,
Viale San Bartolomeo, 400,
19126, La Spezia, Italy

***Abstract*—In the MCM (Mine Counter Measure) context, a lot of effort has been put in imagery systems and especially in high frequency sonar. The latest generation of sonar, SAS (Synthetic Aperture Sonar) systems, has been developed in the last 15 years and provides a new powerful tool for mine detection, identification and classification. The main advantage of SAS systems is a resolution close to the wavelength even at long range. A high frequency SAS system has been developed at NURC, the MUSCLE vehicle (300kHz centre frequency) but, despite the extremely good quality of the SAS images, ambiguities between mine-like objects cannot always be resolved. This study investigates how low frequency SAS systems (LF-SAS) could address the two main limitations of the present systems linked essentially to the sound absorption at high frequencies: providing imagery inside the target and detecting buried targets. Synthetic SAS images have been generated and studied in order to demonstrate the capability of LF-SAS to provide information of the inside of targets. We demonstrate that the inner resonances of objects are visible and exploitable in these LF-SAS images. Most of the time the reverberation level (RL) of the seafloor is the main limiting factor in the interpretation of sonar images. A computation of the RL has been done using the small perturbation theory on a rough seabed and we demonstrate that the first resonant echoes are still visible relative to the RL.**

## I. Introduction

SAS stands for Synthetic Aperture Sonar and has been developed over the last 15 years. It inherits the technologies developed for SAR (Synthetic Aperture Radar) over the last 40 years. The main idea relies on the fact that for a standard sidescan sonar the along track (cross range), resolution is the ratio between the acoustic wavelength and the length of the antenna. In order to increase the resolution in cross range typical sidescan manufacturers have chosen to work at higher frequency despite the sound attenuation in water at high frequency. Even with very high resolution, ambiguities between a mine-like object and a natural object cannot always be resolved. In this paper, we study a low frequency SAS system (LF-SAS). Our objective is to demonstrate that such a system can provide an inner image of the insonified objects.

The paper is organized as follows. In section II, we explain the principles of SAS imaging and the SAS compression algorithms. Then a design of a LF-SAS system is proposed. In section III, synthetic SAS images of simple objects are computed and we discuss the advantages and disadvantages of a LF-SAS system compared to a HF-SAS system. Section IV describes a model for reverberation noise in SAS images based on small perturbation theory on a rough surface. The reverberation level (RL) is compared to the level of the resonances of spherical targets.

## II. SAS Principles

The principle of SAR/SAS is to artificially increase the length of the antenna thanks to the synthetic aperture antenna algorithm in order to increase the cross range resolution [1]. SAS systems use broadband pulses (essentially chirps) in order to increase the range resolution.

### A. SAS image formation

From the raw SAS data, two compression algorithms are performed to obtain the SAS image. Let $s(t,u)$ be the raw signal. $t$ representing the time, and $u$ the along track parameter. The first compression takes advantage of the broadband pulse used by SAS systems. This compression is a range compression and is computed through a match filtering of the echo (see Eq. 1).

$$s_M(t,u) = s(t,u) * p^*(-t) \tag{1}$$

where $p(t)$ represent the SAS broadband pulse. Note that the incoming pulse is usually a chirp, which maximizes the compression by match filtering [2].

Several algorithms can be used to obtain the cross-range resolution. We will be using the backpropagation algorithm [3]. Each pixel $(x,y)$ in the resulting SAS image is computed thanks to Eq. 2

$$f(x,y) = \int_u s_M \left[ \frac{\sqrt{x^2+(y-u)^2}}{c}, t \right] \mathrm{d}u \tag{2}$$

where $c$ represents the speed of sound in water and $s_M$ is the match filtered echo obtained in Eq. 1. This compression technique takes advantage of the wide beamwidth of the SAS system. A single scatterer is represented in the raw SAS image as a parabola assuming the SAS system flies along a linear track. The backpropagation algorithm sums coherently all the contributions of the scatterer along this parabola.

A SAS has been developed at NURC called MUSCLE. This SAS operates at a central frequency of 300 kHz with around 60 kHz bandwidth. The beamwidth is 7°. The system gives a range of 2 $\times$ 200 m with a fixed precision of around 3 cm. Figure 1 displays a picture of the NURC SAS system MUSCLE and an example of a MUSCLE SAS image.

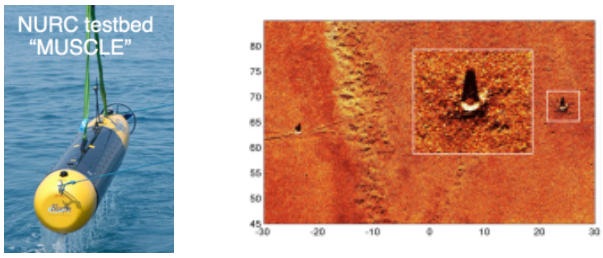


Fig. 1. (*left*) MUSCLE NURC SAS mounted on the Bluefin. (*right*) MUSCLE SAS image of a mine-like object at 65 m range (*courtesy to NURC*).

### *B. Why a low frequency SAS system?*

The images produced by high frequency SAS such as the NURC-MUSCLE are able to provide a centimetric resolution over a range of 200 m. The quality of these images, visually close to optical images, permits difficult tasks such as identification and classification [4]–[7]. Despite the extremely good quality images provided by high frequency SAS, ambiguity between objects can still exist in certain cases. In the context of MCM (Mine Counter Measure), even with high frequency, high resolution systems, distinctions between a sea-mine and a rock can sometimes be difficult. Working with low frequency will inevitably lead to a decrease in resolution, but on the other hand, low frequencies suffer less absorption. By studying a low frequency SAS system, we aim for two main goals:

- produce an internal image of the target
- detect buried targets

The LF-SAS studied in the following sections has the following characteristics:

- Bandwidth: 5 - 50 kHz
- Beamwidth: 90°

According to the RST (resonance scattering theory) [8], the inner resonances of an object are strong when the factor $k.a$ is between 1 and 60. $k = \frac{2\pi f}{c}$ represents the wavenumber, and $a$ represents a characteristic dimension of the object (example: the diameter in the case of a sphere). In our case, we are interested in mine-like objects with a dimension of around 50 cm. The factor $k.a$ of these targets using the LF-SAS frequency band will be included between 10 and 100. We expect strong characteristic resonances.

## III. Synthetic SAS Images of Simple Targets

In this section, we explain how to produce synthetic SAS images of simple targets. Analytical solutions for the back-scattering problem are in most cases unavailable due to the complexity of the sound propagation equations. The problem has been solved only for simple geometrical shaped objects such as spheres [9] or cylinders [10]. We compute synthetic SAS images of simple concentrical sphere objects and compare LF-SAS images with HF-SAS images.

### *A. Synthetic SAS image computation*

In order to compute synthetic SAS images of simple objects such as spherical shells in free water, the first step is to compute the form function $f_\infty$ [9]. From the form function

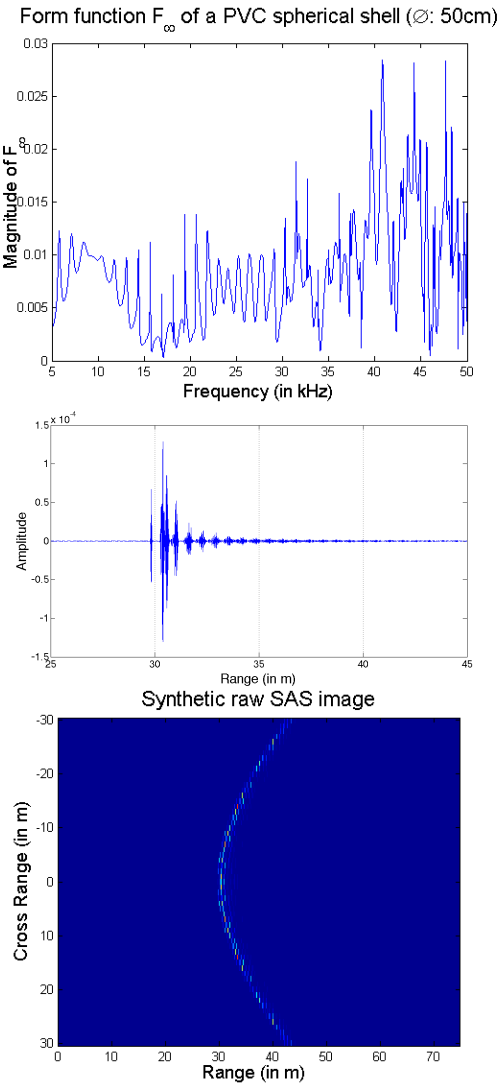


Fig. 2. From *top* to *bottom*: Amplitude of the form function of a PVC spherical shell, its echo in the time domain, synthetic raw SAS data of the target.

$f_\infty$ and the out going pulse $s(t)$, the echo in the time domain of the multi layer sphere can be computed thanks to Eq. 3 [11].

$$p_s(t) = \mathrm{FT}^{-1}\left[\frac{\mathrm{e}^{-2jkr}}{|k|r^2}\mathrm{FT}[s(t)]f_\infty(k)\right] \qquad (3)$$

FT is the Fourier transform and $r$ the range of the target.

Assuming a linear trajectory of the SAS system, the target is constructed in the raw SAS data (*i.e.* before compression) as a parabola. Note that the extension of the parabola depends on the beamwidth of the system. Figure 2 displays the three processing steps described here.

Once the raw SAS data has been computed, the algorithms of compression explained in Section II-A are applied to obtain the synthetic SAS image. Figure 3 shows an example of a synthetic SAS image computed from the results in Figure 2.

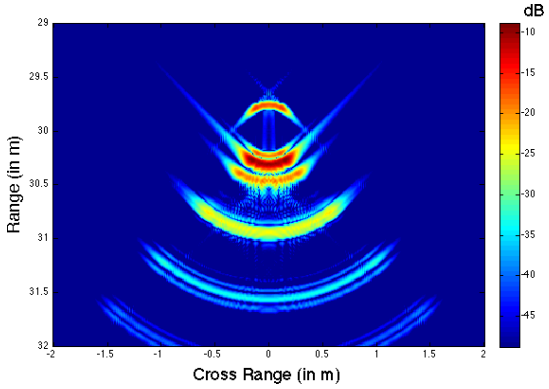


Fig. 3. Synthetic SAS image of a PVC spherical shell (Ø: 50 cm) with the SAS design proposed in Section II-B.

### *B. Comparison between high frequency SAS and low frequency SAS*

In this section we compare synthetic SAS images between a high frequency system and a low frequency system.

*1) A world without sound attenuation:* In an ideal world, we can consider that the absorption is negligible. Figure 4 displays two SAS images from the same target, a PVC spherical shell with 50 cm diameter and 1 cm shell thickness. The low frequency system is the same as that described earlier. The high frequency system has the same beamwidth and a frequency band from 250 kHz to 350 kHz. The pulse for each system is a 100 $\mu$s chirp covering the respective frequency bands of the two systems.

Comparing the two SAS images, the high frequency SAS offers better imagery for several reasons. At higher frequency, the maximum echo level of the sphere increases. For example the maximum echo level of the PVC spherical shell at LF is 50 dB lower than at HF. At higher frequency, more internal waves are excited [12], which offer more characteristics for classification and/or identification.

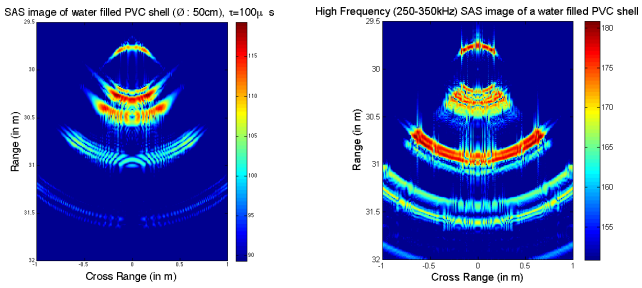


Fig. 4. (*left*) low frequency SAS image of a spherical PVC shell (Ø: 50 cm, wall thickness: 1cm). (*right*) high frequency SAS image of the same target.

*2) Sound attenuation:* The sound suffers from attenuation, especially when it propagates into the seabed or material. At high frequency (above 100 kHz), the main factor for sound attenuation is friction [13]. This attenuation can be introduced in the wave equations by considering a complex sound speed.

Let $p(x)$ be a plane wave:

$$\begin{aligned} p(x) &= \mathrm{e}^{ikx} \text{ with } k = k_r + ik_i \\ &= \mathrm{e}^{ik_r x}.\mathrm{e}^{-k_i x} \end{aligned} \quad (4)$$

In Eq. 4, the first term $\mathrm{e}^{ik_r x}$ corresponds to the equation of a plane wave, and the second term $\mathrm{e}^{-k_i x}$ is a decreasing exponential and models the attenuation of the acoustic wave. Assuming that the amplitude of the imaginary sound speed $c_i$ is much lower than the real part $c_r$ ($|c_i| \ll c_r$ ), $k$ the wave number can be written as:

$$k = k_r + ik_i = \frac{\omega}{c_r} - i\frac{\omega c_i}{c_r^2} \quad (5)$$

Note that $c_i$ is negative.

The attenuation factor $k_i'$ is usually expressed in dB/$\lambda$. It is linked to imaginary sound speed $c_i$ by:

$$c_i = -\frac{k_i' c_r}{40\pi \log_{10} \mathrm{e}} \quad (6)$$

For example, epoxy-resin has the following longitudinal and transversal sound speeds, given with their corresponding attenuation coefficients [14]:

$c_L$ = 3000 m.s$^{-1}$ $\quad \alpha_L$ = 0.8 dB/$\lambda$
$c_T$ = 1550 m.s$^{-1}$ $\quad \alpha_T$ = 1.8 dB/$\lambda$

Thanks to Eq. 6, we can compute the imaginary longitudinal and transversal sound speeds:

$c_L^i$ = -43.98 m.s$^{-1}$
$c_T^i$ = -51.12 m.s$^{-1}$

A typical value for the attenuation coefficients is around 1 dB/$\lambda$, and is frequency independent. So for this reason, low frequency systems suffer less from sound attenuation that high frequency systems. The following table compares the -20 dB attenuation distance for a HF (300 kHz) and a LF (5 kHz) assuming a 1 dB/$\lambda$ attenuation.

| Frequency | $\lambda$ | -20 dB attenuation |
|---|---|---|
| 300 kHz | 5 mm | 10 cm |
| 5 kHz | 30 cm | 6 m |

*3) LF-SAS vs HF-SAS:* As we saw in Eq. 4, the sound attenuation is directly integrated in the wave propagation equations by introducing a complex sound speed (computed thanks to Eq.6). In order to demonstrate the potential of LF-SAS to image inside of the target, a series of simulations has been computed. In this section, two results are discussed.

In the first experiment, we produce a SAS image of an epoxy-resin shell. The outer diameter of the shell is 50 cm and the inner diameter is 10 cm. The shell is filled with air. The drawing in figure 5 shows the configuration and the geometry of the target.

SAS images have been computed using the algorithm discussed in section III-A. The sound attenuation has been taken into account according to the equations introduced in section III-B2, as well as the values for the imaginary longitudinal and transversal sound speed for the epoxy-resin.

LF-SAS images and HF images have been computed. The HF-SAS system has the same beamwidth as the LF-SAS system and covers a frequency band from 250 kHz to 300 kHz. The reason for using a slightly lower frequency band than the HF-SAS described in section III-B1 is linked to the instability of the Bessel functions for high values.

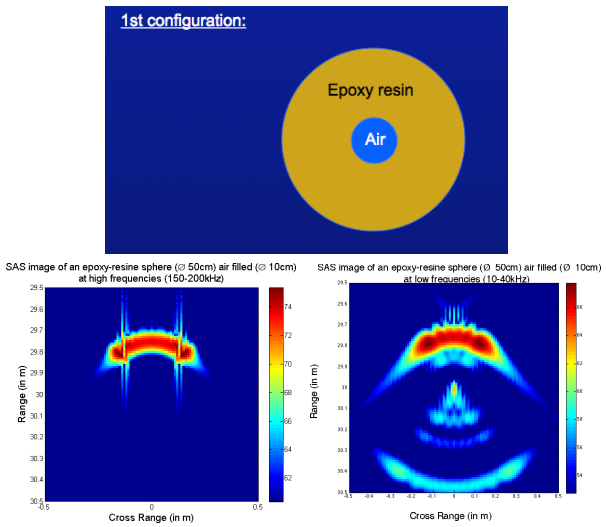


Fig. 5. (*top*) Geometry of the epoxy-resin spherical shell (outer Ø: 50 cm, inner Ø: 10 cm), the sphere is filled with air. (*bottom-left*) HF-SAS image of the sphere. (*bottom-right*) LF-SAS image of the same target.

The resulting synthetic HF-SAS and LF-SAS images displayed in figure 5 show the capability for LF-SAS to image inside the target. The air inside the epoxy-resin sphere is acoustically highly reflective, but because of the strong attenuation of the high frequencies, the HF-SAS cannot image inside the sphere, and only the front face of the sphere appears in the SAS image.

On the other hand, the LF-SAS image shows the inside of the target and its resonances. The difficult part here is to be able to interpret this image. As can be seen in Eq. 2, the reconstructed image (which is a range image) is based on the hypothesis of a constant sound speed $c$, which is the sound speed in water. Inside the epoxy-resin spherical shell, the sound travels faster (around 3000 m.s$^{-1}$ for the longitudinal wave). In this case the target in the image appears deformed and loses its circle shape. What is appearing to be the centre of the sphere is in fact the back face of the target. The air structure inside the object is situated between the front and back echoes.

The second simulation tries to model a mine like object more accurately. A shell of fibreglass of 1 cm thickness surrounds a layer of water and the explosive part is modelled by a a layer of epoxy-resin. The electronics box is represented by a inner core layer of air. A diagram of this model is shown in Fig. 6 (*top*). In this simulation, the sound absorption within the fibreglass and the epoxy-resin has been taken into account.

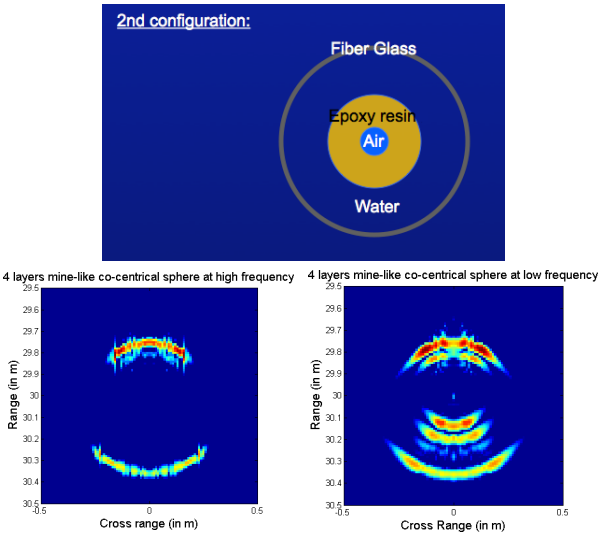


Fig. 6. (*top*) Geometry of the co-centrical *"mine-like"* spheres. (*bottom-left*) HF-SAS image of the target. (*bottom-right*) LF-SAS image of the same target.

| parameters for epoxy-resin | |
|---|---|
| $c_L$ = 3000 m.s$^{-1}$ | $c_L^i$ = - 43.98 m.s$^{-1}$ |
| $c_T$ = 1550 m.s$^{-1}$ | $c_T^i$ = - 51.12 m.s$^{-1}$ |
| **parameters for fibreglass** | |
| $c_L$ = 3000 m.s$^{-1}$ | $c_L^i$ = - 19.24 m.s$^{-1}$ |
| $c_T$ = 2550 m.s$^{-1}$ | $c_T^i$ = - 20.00 m.s$^{-1}$ |

In the HF-SAS image (Fig. 6 (*bottom-left*)), the sphere appears empty. The LF-SAS system allows an inspection inside the target. The echoes of the core structure of the *mine-like* object are clearly visible.

## IV. Reverberation Level in SAS Images

In the previous sections, echoes of multi-layers spheres have been computed in free water. However in sidescan sonar or SAS systems, the main limiting factor in terms of noise comes from the reverberation level (RL). The RL is not noise in the sense that it contains information relative to the reflectivity and the geometry of the seabed, but it represents a coherent noise from a signal processing and image processing point of view. A model of RL suitable for SAS is studied. The main idea is to compare the SAS-RL to the level of the secondary echoes for the simple targets studied in section III.

### A. Small Perturbation Fluid Model

The model chosen here is based on the small perturbation fluid model [15]. The interface between the water and the sediment is denoted $\zeta(x, y)$. $\zeta$ represents the roughness of the seabed. The seabed is considered as flat: meaning that $\zeta(x, y)$ has zero mean. The term *"small perturbation"* relates to a rough flat seabed hypothesis. The roughness of the interface $\zeta$ is supposed to be smaller than the wavelength. Note that for 10 kHz frequency, the wavelength corresponds to 15 cm.

The water column (represented by the half-space: $\{z > \zeta(x, y)\}$) is considered as homogeneous. Let $c_1$ be its sound speed, and $\rho_1$ its density. The sound attenuation in water is neglected. The bottom (represented by the half-space: $\{z \leq$

$\zeta(x,y)\}$) is also considered as a homogeneous fluid with a sound speed $c_2$ and a density $\rho_2$. The sound attenuation in the sediment $\delta$ is assumed linear relative to frequency, so it can be expressed as dB/$\lambda$.

Let $k_1$ and $k_2$ be respectively the wave number in water and in the sediment.

$$k_1 = \frac{2\pi f}{c_1} \quad (7)$$

$$k_2 = \frac{2\pi f(1+i\delta)}{c_2} \quad (8)$$

Using the first order perturbation, the scattered field $\phi$ can be expressed as:

$$\phi(f) = -S(f)\frac{k_1^2}{2\pi}\iint B(x',y')\tau(x',y')\zeta(x',y')\frac{e^{ik_1(r_s+r_r)}}{r_s r_r}dx'dy' \quad (9)$$

where $S(f)$ is the Fourier transform of the outgoing pulse, $B$ represents the cross beampattern (transmitter/receiver), $r_s$ and $r_r$ are respectively the distance between a point in the interface $(x',y',\zeta(x',y'))$ and the source and the distance between the same point $(x',y',\zeta(x',y'))$ and the receiver. $\tau$ is the first order perturbation scattering parameter, and its expression is:

$$\tau(x,y) = \frac{1}{2}(1+V_s)(1+V_r)G \quad (10)$$

with

$$\kappa = (1+i\delta)\frac{c_1}{c_2}$$

$$\rho = \frac{\rho_2}{\rho_1}$$

$$G = \left(\frac{1}{\rho}-1\right)\left(\cos\theta_r\cos\theta_s\cos\phi - \frac{P_r P_s}{\rho}\right) + 1 - \frac{\kappa^2}{\rho}$$

$$P_{s,r} = \sqrt{\kappa^2 - \cos^2\theta_{s,r}}$$

$$V_{s,r} = \frac{\rho\sin\theta_{s,r} - \sqrt{\kappa^2-\cos^2\theta_{s,r}}}{\rho\sin\theta_{s,r} - +\sqrt{\kappa^2-\cos^2\theta_{s,r}}}$$

$\phi$ is the bistatic angle. $\phi = \pi$ corresponds to the back-scattering case, $\phi = 0$ to the forward-scattering case.

The advantage of this model is its simplicity. The scattered field in Eq. 9 is an integration through the insonified interface of geometrical parameters and works directly with 3D surfaces. The computation is very quick in comparison to trying to solve the wave equation at the interface for example.

In order to compute a SAS image of a particular seafloor, we first generate the rough surface between the water column and the sediment. Since the mid-seventies, it has been shown that a lot of natural structures can be well represented by fractal models [16]. For this reason, the model used to generate the seafloor is based on fractals. The generation of the 3D rough seabed surface is done using a pink noise method [17]. Figure 7 displays an example of a rough surface generated using fractals.

Once the roughness $\zeta$ is computed, Eq. 9 is solved for all the frequencies within the bandwidth used by the SAS system.

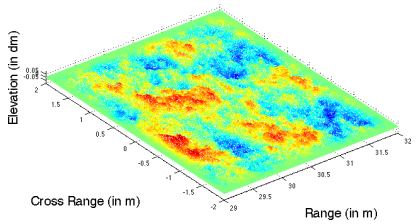


Fig. 7. Example of rough surface generated using a pink noise method.

The time domain echo is obtained by applying the inverse Fourier transform to $\phi(f)$. This process is repeated along the trajectory of the SAS system in order to synthesise the raw SAS data. The algorithms explained in section II-A are applied to the raw data to construct the final SAS image.

### *B. Results*

*1) Reverberation Level and SNR estimation:* Figure 8 displays the roughness $\zeta$ computed from a fractal generator, and the resulting SAS image from the rough surface. Figure 8 (*bottom*) displays the histogram associated to the patch of seabed imaged with the SAS system.

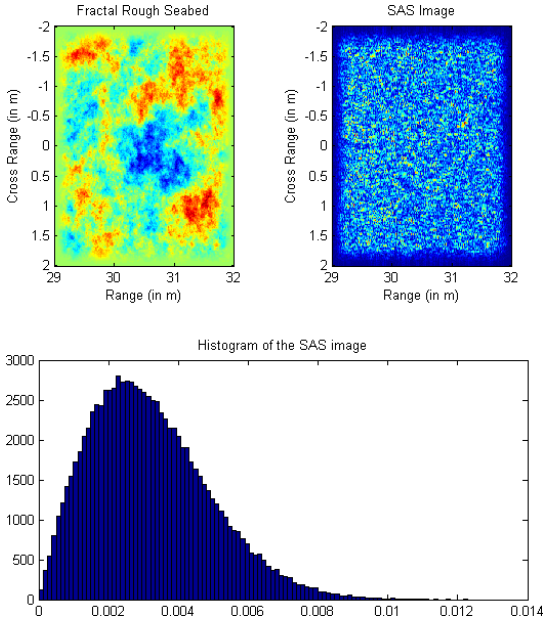


Fig. 8. *top-left* Example of rough surface generated using a pink noise method. *top-right* SAS image computed from the rough seabed. *bottom* Histogram associated with the seabed SAS image.

The histogram of the patch of synthetic SAS image has been computed in order to evaluate the RL and RL distribution. The synthetic RL distribution follows a Rayleigh distribution. This first texture feature matches with the real SAS-RL.

We want here to compare the RL to the level of the different secondary echoes of a target of interest. As an example we will work here with the PVC spherical shell (Ø: 50 cm, wall-thickness: 1 cm) we have already studied earlier (in section III). In figure 9 the synthetic SAS image of the PVC spherical shell in free water (*left*) and the histograms of the

RL and the different parts of the highlight of the object are displayed.

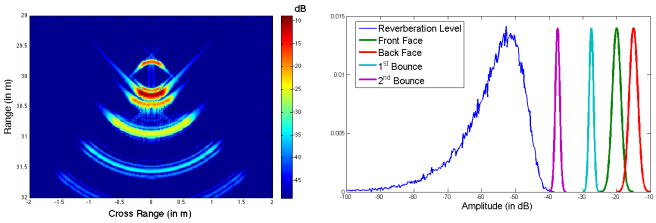


Fig. 9. (*left*) synthetic SAS image of the PVC spherical shell in free water. (*right*) histogram of the RL and the different parts of the echo of the PVC spherical shell.

We are comparing here a target in free water and the RL from a flat featureless seabed. For this PVC target, and as shown in figure 9, the highlights from the front face and back face are clearly visible (more than 30 dB above the RL mean value). The first two secondary echoes are visible as well (respectively 20 and 10 dB above the RL). The following resonating echoes disappear into the reverberation level noise.

In conclusion, with a LF-SAS the structure of the highlight of the target, induced by its geometry, is highly visible with respect to the reverberation level, but also some of the secondary echoes coming a resonating target can be imaged. This will provide a strong feature for detection, classification and identification.

## V. Conclusions

Sonar manufacturers have mainly been considering high frequency for imaging systems. The reason behind this choice is clearly the resolution gain. The resolution is indeed directly linked to the wavelength (inversely proportional to the frequency). HF-SAS, such as the NURC-MUSCLE system, provides sonar images with a centimetric resolution.

As discussed in section III-B2, the main disadvantage of the high frequencies is the strong attenuation within solid materials or even the seabed. LF-SAS systems on the contrary can provide images of the resonances of the targets and can image the inside of the insonified objects. Using the same argument about sound absorption, buried targets can be detected using a low frequency system.

One of the disadvantages of the LF-SAS is a lower quality image compared to a HF-SAS system. A second disadvantage will be the difficult interpretation of LF-SAS images. As seen in III-B3, the LF-SAS image of a particular target will be distorted by the difference between the sound speed in water and within the target. If the sound speed of the material is assumed *a priori* unknown, the true geometry of the inside of the target is not available. However it will be possible to distinguish between an empty object and a non-empty object.

Future generations of sonar may use both high and low frequencies for respectively high quality images and inner target insonification.

## Acknowledgment

This work was supported by NURC and EPSRC under research contracts EP/H012354/1. We also acknowledge support from the Scottish Funding Council for the Joint Research Institute in Signal and Image Processing between the University of Edinburgh and Heriot-Watt University which is a part of the Edinburgh Research Partnership in Engineering and Mathematics (ERPem).

## References

[1] K. Tomiyasu. Tutorial review of synthetic-aperture radar (sar) with applications to imaging of the ocean surface. *IEEE Proc.*, 66(5):563 – 583, may 1978.

[2] G. Turin. An introduction to matched filters. *Information Theory, IRE Transactions on*, 6(3):311 –329, june 1960.

[3] J.A. Seydel. Ultrasonic synthetic-aperture focusing techniques. In New York: Academic Press, editor, *NDT Research Techniques for Nondestructive Testing*, 1982.

[4] P. Courmontagne. A new approach for mine detection in sas imagery. In *OCEANS 2008 - MTS/IEEE Kobe Techno-Ocean*, pages 1 –8, 8-11 2008.

[5] M. Jonsson, J. Pihl, and M. Aklint. Imaging of buried objects by low frequency sas. In *Oceans 2005 - Europe*, volume 1, pages 669 – 673 Vol. 1, 20-23 2005.

[6] A.D. Matthews, T.C. Montgomery, D.A. Cook, J.W. Oeschger, and J.S. Stroud. 12.75" synthetic aperture sonar (sas), high resolution and automatic target recognition. In *OCEANS 2006*, pages 1 –7, 18-21 2006.

[7] M. Pinto, A. Bellettini, R. Hollett, and L. Wang. Recent advances in synthetic aperture sonar for proud and buried object detection. *J. Acoust. Soc. Am.*, 111(5):2457–2457, 2002.

[8] G.C. Gaunaurd and H. Uberall. RST analysis of monostatic and bistatic acoustic echoes from an elastic sphere. *J. Acoust. Soc. Am.*, 73(1):1–12, 1983.

[9] R.R. Goodman and R. Stern. Reflection and transmission of sound by elastic spherical shells. *J. Acoust. Soc. Am.*, 34(3):338–344, 1962.

[10] R.D. Doolittle and H. Uberall. Sound scattering by elastic cylindrical shells. *J. Acoust. Soc. Am.*, 39(2):272–275, 1966.

[11] R. Hickling. Analysis of echoes from a solid elastic sphere in water. *J. Acoust. Soc. Am.*, 34:1582–1592, 1962.

[12] Alessandra Tesei, Warren L. J. Fox, Alain Maguer, and Arne Løvik. A method of target characterization based on the analysis of scholte–stoneley and lamb-type waves scattered by submerged fluid-filled thin-walled shells. *J. Acoust. Soc. Am.*, 103(5):2813–2813, 1998.

[13] Philip L. Marston. Gtd for backscattering from elastic spheres and cylinders in water and the coupling of surface elastic waves with the acoustic field. *J. Acoust. Soc. Am.*, 83(1):25–37, 1988.

[14] Alessandra Tesei, Piero Guerrini, and Mario Zampolli. Tank measurements of scattering from a resin-filled fiberglass spherical shell with internal flaws. *J. Acoust. Soc. Am.*, 124(2):827–840, 2008.

[15] M. D. Richardson and D. R. Jackson. *High-Frequency Seafloor Acoustics*. Springer, 2006.

[16] B. Mandelbrot. *The fractal geometry of nature*. W H Freeman & Co, 1982.

[17] Alex P. Pentland. Fractal-based description of natural scenes. *IEEE Trans. Pattern Anal. Machine Intell.*, PAMI-6(6):661–674, Nov. 1984.